Enhanced Active and Reactive Power Sharing in Islanded Microgrids

Mehdi Parvizimosaed, *Student Member, IEEE,* Weihua Zhuang, *Fellow, IEEE*

***Abstract*—The intermittency of renewable energy makes the control of islanded microgrids (MGs) more difficult than that of the grid-connected mode. In conventional methods, the controller is designed to regulate the system frequency and voltage only based on the droop control theory. Consequently, the system frequency and voltage regulation are mostly provided by the fast response distributed generators (DGs), e.g. energy storage systems (ESSs). This controller design will reduce the availability of DGs with lower droop gains for future dispatches. The main novelty of this paper relies on proposing an intelligent power sharing (IPS) approach to regulate the system frequency and voltage based on DGs' operating power capabilities and their droop control gains. The communication infrastructure is involved in the proposed IPS to diminish the dependency on fast response DGs. Moreover, the IPS is equipped with an adaptive virtual impedance to reduce the impact of coupling between the active and reactive power on the voltage regulation. The performance of the controller is evaluated through different simulation studies based on a 14-bus CIGRE test system. Time-domain simulations prove the effectiveness of the IPS approach in achieving acceptable frequency and voltage regulation along with high power sharing accuracy. Also, a small-perturbation stability analysis is developed to study the IPS control robustness under different scenarios.**

***Index Terms*—Islanded microgrid, intelligent power sharing, stability, frequency/voltage control.**

NOMENCLATURE

Indices and Superscripts

i, j, g	DG assets
b	Bus asset
l	Line signal
o	Output signal
p	Power controller
v	Voltage controller
c	Current controller
lcl	LCL filters
SG	SG
INV	Inverter unit
Ld	Load superscript
Ln	Line superscript

Sets

$\mathcal{G}$	DG
$\mathcal{N}$	Bus

Parameters

n_G	Number of DGs
n_{Ld}	Number of loads
n_{Ln}	Number of lines
ω_0	Reference frequency of the system (rad/s)
ω_n	Nominal frequency of the system (rad/s)
ω_{ss}	Steady-state frequency of the system (rad/s)
ω_c	Cut-off frequency of LCL filter (rad/s)
ω_{com}	Common frame frequency of inverter (rad/s)
s, ω	Laplace variable
$\Delta\omega$	Frequency change (rad/s)
P_i	Output active power output of DG i (kW)
Q_i	Output reactive power output of DG i (kW)
$\overline{P_i}/\underline{P_i}$	Maximum/Minimum output active power of DG i (kW)
$\overline{Q_i}/\underline{Q_i}$	Maximum/Minimum output reactive power of DG i $(kVAr)$
P_L	Load power (kW)
K_t, T_t	Turbine gain and time constant of SG (s)
K_g, T_g	Governor gain and time constant of SG (s)
K_s, T_s	Sensor gain and time constant of SG (s)
K_e, T_e	Exciter gain and time constant of SG (s)
K_A, T_A	AVR gain and time constant of SG (s)
H	Inertia constant (J/kVA)
$v_{o,dq}$	Output voltage in $dq-$axis (V)
$i_{o,dq}$	Output current in $dq-$axis (A)
$i_{l,dq}$	Current flowing the coupling inductor in $dq-$axis (A)
W_f	Weighted adjacency matrix of frequency control
W_v	Weighted adjacency matrix of voltage control
K_i	Frequency IPS gain DG i
κ_i	Voltage IPS gain DG i
$K^f_{i,tr}$	Frequency-transient IPS coefficient of DG i
$K^v_{i,tr}$	Voltage-transient IPS coefficient of DG i
β_i	V-Q compromise IPS gain of DG i
m_{pi}	Frequency droop value of DG i (Hz/kW)
n_{pi}	Voltage droop value of DG i $(V/kVAr)$
S_v	Slack variable of voltage integration (V)
x	State variable
u_x, u_y	Input vector of state-space model
r_v	Resistance of virtual impedance (Ω)
L_v	Inductance of virtual impedance (H)
Z_v	Virtual impedance (Ω)
z_{ij}	Impedance of line between node i and j (Ω)
y_{ij}	Admittance of line between node i and j (Ω)
ϕ_{ij}	Phase of Impedance z_{ij} (rad)
θ_i	Phase voltage of bus connected to DG i (rad)
f_{zv}	Virtual impedance sensitivity function
R_N	Virtual resistor matrix in stability analysis (Ω)
υ, γ	State variable of current/voltage controller in inverter
S_λ	Stability sensitivity index
S_m	Stability margin index
Ψ_j	Stability margin of controller j
M_G	Adjacency matrix of DGs to nodes
M_{Ld}	Adjacency matrix of loads to nodes
M_{Ln}	Adjacency matrix of MG network to nodes
t_{set}	Settling time (s)

The authors are with the Department of Electrical and Computer Engineering, University of Waterloo, Waterloo, ON N2L 3G1,Canada (e-mail: m3parviz@uwaterloo.ca; wzhuang@uwaterloo.ca).

I. INTRODUCTION

DUE to economic problems and technical issues in electric power grids, macro-beneficiaries are driving the energy sector towards the introduction of smart grids [1]. Within a smart grid, a microgrid

(MG) is a low-voltage distribution network consisting of a variety of distributed generators (DGs), energy storage systems (ESSs), and both controllable and uncontrollable loads, and operates in 1) grid-connected and 2) islanded modes [2]. The power sharing approach in islanded MGs is more challenging than that of grid-connected mode because of the low inertia feature of MGs and capacity limitations of DGs. Due to the dynamics of renewable resources and load variations, an imbalance between supply and demand causes frequency and voltage deviations [3]. Mismatched power can be balanced by power sharing, which mainly affects a) MG stability margins, b) frequency and voltage restoration, c) the operating power capability of DGs [4], and d) optimal operation of MGs [5]. The existing power sharing approaches involve either a) droop power sharing control or b) isochronous power sharing control.

A. Literature Survey

In droop power sharing, DGs mimic the behavior of synchronous generators (SGs) in conventional power systems and share the power mismatch in proportion to their droop values. Most recent studies have examined approaches such as conventional power-frequency (P-f) [6], transient control [7], load-angle [8], and resonance-based droop controllers [9]. All these methods are built on top of the conventional droop control mechanisms, which damp oscillatory modes of power sharing controllers and reduce the steady-state frequency and voltage errors. However, with an increase in the span of islanded MG operation, it is imperative to regulate frequency and voltage of MG not only stably, but also optimally [10]. These approaches result in MG instability when the droop values of DGs are increased to share the mismatched power among the DGs. In the special cases, increasing the operating power in DGs is not possible anymore when they reach their rated power. Hence, the choice of droop coefficients has a significant impact on frequency and voltage limit as well as power sharing accuracy [11]. In contrast to the limitations of droop control, isochronous power sharing methods provide zero steady-state frequency and voltage errors. They share the active and reactive power according to DGs rated power. Although isochronous power sharing approaches address the challenge of MG instability, they suffer from slow power sharing control, causing improper frequency and voltage regulation [12]. To overcome these problems, the dynamic droop controller adaptively changes the droop gain to handle the increase in frequency deviation. Due to the high penetration of SGs in islanded MGs, which have relatively big inertia constant, dynamic droop controller can not maintain the stability, especially in subject to large disturbances [13]. Some studies deal with these issues by introducing a supplementary loop and diffusive averaging variables that promote fast and smooth frequency regulation. Diffusive averaging algorithms integrate proportional and integral diffusive variables into conventional models. These algorithms utilize the communication infrastructure in the primary control level to regulate the frequency precisely [14]. However, these approaches cannot share power uniformly among DGs while still maintaining MG stability. Besides, a supplementary loop has been introduced to regulate the MG frequency by adding the virtual inertia to MGs. However, this method is restricted by the speed/power rating and recovery period of generators/turbines [15]. Further challenges arise from the compromise between voltage regulation and reactive power sharing. In the low voltage MGs, line inductance value is considerably small with resistive cable behavior and normally has a low X/R ratio [16]. Decoupling between the active and reactive power is performed by the compensation of line impedance connected to DGs [17].
The virtual impedance loop as a potential solution performs in MGs with mismatched inductive/resistive feeder impedance, to enhance

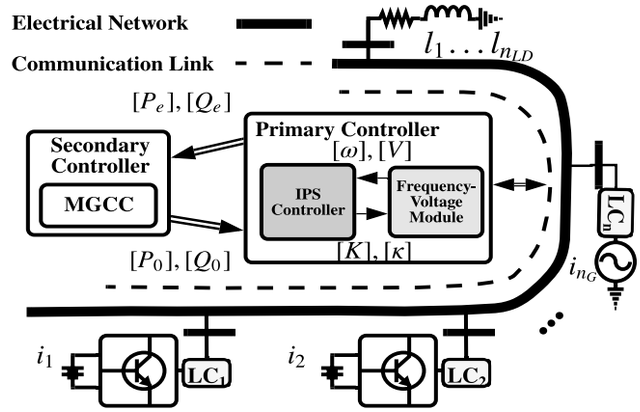

Fig. 1. Low-detail configuration of an MG with communication network.

the power sharing accuracy. The focus has been on the mismatch in the output impedances of the closed-loop controlled inverters. This compensation performs properly for a single generator connected to the power common coupling bus but does not work if there are multiple generators. To address this issue, various approaches have been introduced, such as inductive virtual impedance [18], virtual impedance adapted to the sensitivity factor of active power/reactive power [19], and virtual impedance calculated by injection of a small AC voltage signal to a common bus [20]. These approaches result in accurate power sharing if knowledge of the feeder impedances is available for different operating load changes. However, load changes during or between the compensation periods lead to poor power sharing [21]. As the summary, the design of a new power sharing approach is necessary to overcome the drawbacks mentioned above.

B. Contributions and Paper Outline

The objective of this paper is to determine an intelligent power sharing (IPS) approach that allows for dispatching the active and reactive power among DGs based on their droop control gains and operating power capabilities. The IPS approach is designed to improve the frequency and voltage regulation. A small-perturbation stability analysis is developed to determine the required conditions for the proposed controller gains. Specifically, the proposed IPS approach offers the following novelties:
1) Accurate active and reactive power sharing of DGs based on their droop values and operating power capabilities which improves the life-cycle of fast-acting dispatchable units;
2) Robust performance under rapid load/renewable energy variations while maintaining the MG frequency and voltage stability;
3) A Dynamic compromise between voltage regulation and accurate reactive power sharing among DGs;
4) An adaptive virtual impedance to mitigate the impact of coupling between active and reactive power on the voltage regulation.
The remainder of this paper is organized as follows. Section II describes the system model. Section III presents the proposed power sharing model for islanded MGs. The stability analysis is presented in Section IV. Numerical results are given in Section V. Section VI concludes this research work.

II. System Model and Problem Description

Consider an islanded MG over a distribution network consisting of a cluster of DGs $i := \{1, 2, ..., n_G\}$, loads $Ld := \{l_1, l_2, ..., l_{n_{Ld}}\}$, connected together within an AC link. Fig. 1 depicts that local controllers (LCs) of DGs are in charge of controlling the frequency and voltage as well as ensuring a reliable and stable operation.
These LCs are modeled as a architecture that does not need a

main grid central controller (MGCC) [22]. Any change in DG power variable and/or net electrical power demand, represented as total power variation, results in a frequency change. In the frequency control, DGs and controllable loads change their generation/consumption power using droop theory. LCs are designed to allow the steady-state frequency to drop below the nominal value when the load increases or the power generation of non-controllable units decreases. This frequency drop is modeled as speed regulation or droop value. Hence, DGs can change their reference set points (P_0) to contribute to the frequency control (called P-f droop control). In the voltage control, the reactive power sharing among different DGs is achieved through the control of DG output voltage magnitude. Islanded MG components are grouped into three main classes:

1-Inverter-based Generators: Most DGs, such as energy storage and photovoltaic resources, operate as the DC generators connected to the AC link via DC/AC inverters. The controller of each individual inverter consists of power, voltage, and current controller modules, as well as LCL filters. The system control is categorized into cascaded control loops, i.e., the power control loop and the voltage/current control loop, to ensure stable operating conditions [23]. A low-pass filter with a cut-off frequency is used to filter the ripple components when calculating the active and reactive power. Then, a V/f reference generator changes the reference active/reactive power to compensate for the possible variations of frequency and voltage in the AC link. The conventional voltage and frequency controllers work based on the droop slope and deviation of the active and reactive power from their reference set points ($P-P_0$ and $Q-Q_0$) [11]. Under the voltage control paradigm, the output active power and the voltage reference set-points are fed to a current reference generator to obtain the d- and q-axis reference current set points [12].

2-Synchronous Generators: The synchronous generators (SGs), such as micro-turbine and diesel generators, can be directly connected to the MG. A typical SG consists of different components, i.e., a governor, turbine, and AC machine. The frequency in an SG changes subject to the difference between the driving mechanical and developed electrical power in line with swing theory. In this model, electric power is sensitive to frequency changes because of the inductive behavior of AC loads. The turbine and governor are in charge of frequency regulation [11]. A similar convention is applied to regulate the voltage by sensor, exciter, automatic voltage regulator, and stator/rotor of SG.

3-Frequency-Voltage Dependent Load: The loads in MGs are typically modeled by a voltage-dependent equation and can be viewed as equivalent to a ZIP load. According to the load voltage-dependent model presented in [8], the loads operate at their nominal voltage prior to any voltage change ΔV, and thus load change $\Delta P_L = ((1+\Delta V)^{1.5}-1)P_{L0}$, where P_{L0} is the active power under nominal operating condition [25]. In general, the voltage change is very much dependent on load characteristics. The relation between changes in voltage and frequency can be derived from [8] as $\Delta V = (-2\Delta\omega \times H/(\omega_0 P_{L0})+1)^{0.6}-1$. A comprehensive study is carried out to model frequency-voltage dependent loads that proves these equations [26]. Note that a generator with a higher droop control value contributes less in compensating for load perturbations in the MG. Care should be taken to tune the droop controller so as to avoid making the DGs generate power close to their full-load rating. As an illustration, Fig. 2 shows the uniform active/reactive power sharing to regulate frequency and voltage with two DGs. Under the conventional power sharing paradigm, active power of DG_2 reaches the maximum value ($\overline{P}_{DG_2}$) which is unrealistic. In addition, the application of uniform voltage-regulating ensures that both DG voltage magnitudes are restored to a common steady-state voltage (V_0^1). However, different reactive power injections and line impedance effects cause bus voltages to deviate from the common value. It is concluded that an ideal power sharing controller should allow for a tuneable compromise between the frequency/voltage regulation speed and DG operating power capability. It should also keep the voltage between upper and lower limits, while maintaining accurate reactive power sharing.

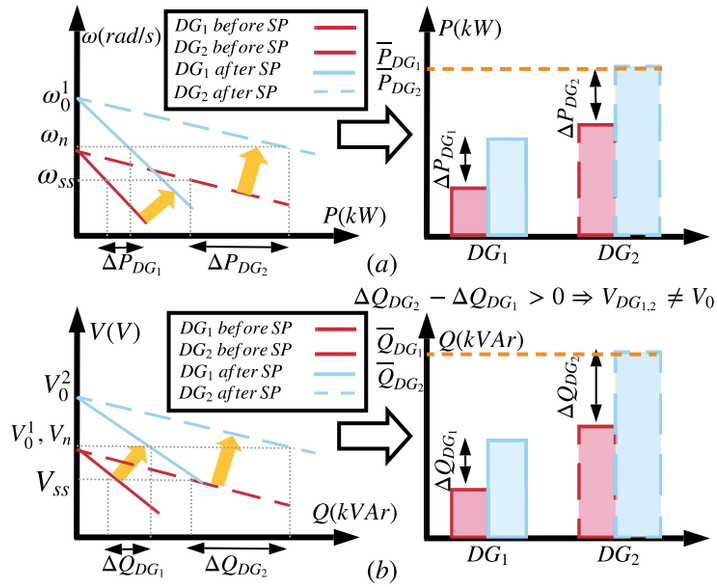

Fig. 2. Conventional secondary controller for (a) active (b) reactive power sharing before/after shifting process (SP).

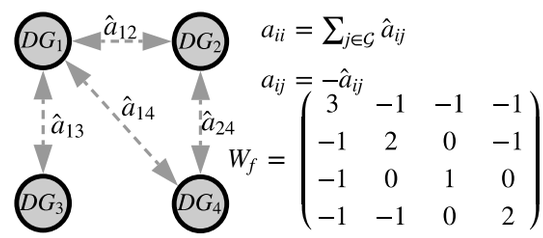

Fig. 3. Frequency adjacency matrix and corresponding graph for four DGs.

III. Intelligent Power Sharing Controller

The intelligent power sharing (IPS) controller relies on the communication network to propagate DGs parameter information including operating and rated power and droop controller gain. This controller leads to the proper frequency and voltage regulation, accurate active power sharing, and tuneable trade-off between voltage regulation and reactive power sharing. This architecture aims to reduce the steady-state frequency and voltage errors with the introduction of control signals. The communication structure among the DGs is described by a weighted frequency adjacency matrix ($[W_f]$) in the order of $n_G \times n_G$ with elements $a_{ij} = a_{ji}$. For instance, if two frequency-controllable units, i and j, are connected, arrays of adjacency matrix are $a_{ij} = -\hat{a}_{ij} = -1$. The same convention is applied to voltage adjacency matrix ($[W_v]$), where LCs in charge of reactive power sharing communicate together to maintain the voltage regulation. The voltage adjacency matrix can be different from frequency one due to the characteristics of DGs in power sharing. The IPS control relies on the control signals to unevenly shift the P-f and Q-V droop curves to achieve better power sharing among DGs. This uneven shifting process requires that neighbouring DG units exchange information to act secondary control. Observe in Fig. 4 that the uneven shifting approach shares the uniform active and reactive power to maintain both frequency/voltage regulation speed and DG operating power capability.

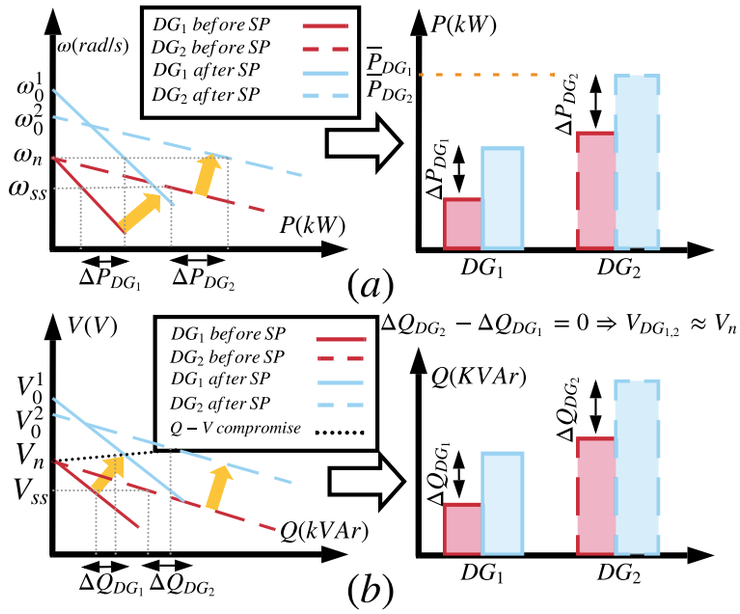

$\Delta Q_{DG_2} - \Delta Q_{DG_1} = 0 \Rightarrow V_{DG_{1,2}} \approx V_n$

Fig. 4. Uneven SP for (a) active (b) reactive power sharing.

A. Power Flow Constraints

Define impedances $z_{ij} = |z_{ij}|\angle -\phi_{ij}$ for angles $\phi_{ij} \in [-\pi/2, \pi/2]$ for all $\{ij\} \in \mathcal{N}$, admittance matrix Y with elements $y_{ij} = y_{ji} = -1/z_{ij}$ for $i \neq j$, and $y_{ii} = \sum_{j\in\mathcal{G}} 1/z_{ij}$. Each bus is associated with an electrical injection $S_{e,i} = P_{e,i} + jQ_{e,i}$, and voltage phasor $V_i\angle\theta_i$ with $V_i > 0$. The active and reactive nodal power injections are given by

$$P_{e,i}(\theta_i) + jQ_{e,i}(\theta_i) = \sum_{j\in\mathcal{G}} Y_{ij}V_iV_je^{(\phi_{ij}-\theta_i-\theta_j)} \tag{1}$$

It is noteworthy to mention that the conventional Newton Raphson method has certain issues such as lack of slack bus, sparse admittance matrix in the case of inverter-based MG, and the inconsistency of voltage and frequency due to droop characteristics. Hence, the IPS approach uses the modified Newton Raphson (MNR) with taking account the droop characteristics of DGs. The theory behind of MNR is the consideration of a mismatch power matrix and corresponding Jacobian matrix in an iteration process. This algorithm aims to converge the mismatch power matrix to zero [24].

B. IPS Control for Frequency Regulation

The control signal achieved from the frequency change ($\Delta\omega$) aims to reduce the steady-state error and shifts the droop curve. As illustrated in Fig. 5, $[K]$ is a diagonal matrix illustrating the fraction of contribution in the frequency control based on DG power generation capability and droop values ($m_{pi} > 0$), given by

$$k_{ii} = \frac{(\overline{P}_i - P_{e,i})/m_{pi}}{\sum_{j\in\mathcal{G}}(\overline{P}_j - P_{e,j})/m_{pj}}, \qquad i \in \mathcal{G}. \tag{2}$$

The LCs communicate with each other by frequency adjacency matrix to improve the MG stability by having the same control signal, $(K_{tr}^f sI + [W_f])^{-1}\Delta\omega(s)$, for all committed DGs. This correction is to shift all droop control curves by a coefficient based on $\omega_n - \omega_{ss}$, for the desired active power sharing. In addition, a frequency-transient coefficient is added to the control variable in order to adjust the speed of frequency restoration. For instance, a smaller K_{tr}^f corresponds to a slower transient frequency response. Updating the IPS frequency controller gain achieves the active power sharing among DGs, with consideration of frequency regulation speed ($1/m_{pi}$) and DG operating power capability ($\overline{P}_i - P_{e,i}$).

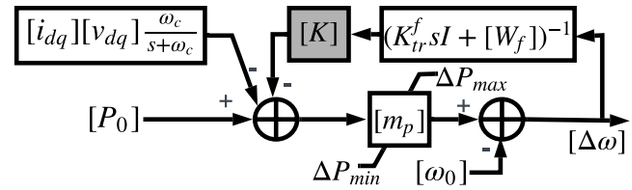

Fig. 5. The diagram of frequency controller in the IPS control with limits on active power change ($\Delta P_{min}, \Delta P_{max}$).

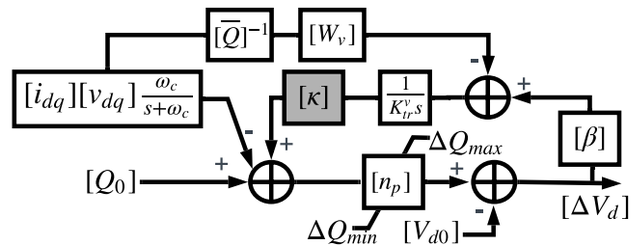

Fig. 6. The schematic of voltage-regulating IPS control bounded by reactive power changes ($\Delta Q_{min}, \Delta Q_{max}$).

C. IPS Control for Voltage Regulation

The IPS controller is to achieve a trade-off between reactive power sharing and voltage regulation. As illustrated in Fig. 6, each DG generates reactive power is the proportional to its rated reactive power. It regulates the voltage based on a control signal, which consists of the voltage error ($V_{di} - V_{d0}$) and reactive power sharing of DGs. To make a trade-off between the output voltage and reactive power sharing, voltage regulating controller uses the information of $(Q_i/\overline{Q}_i - Q_j/\overline{Q}_j)$ and a Q-V compromise coefficient matrix $[\beta]$. Similar to frequency consensus, a diagonal matrix $[\kappa]$ is defined as the fraction of DG contribution in the voltage regulation based on operating reactive power capability and voltage droop value, $n_{pi} > 0$, given by

$$\kappa_{ii} = \frac{(\overline{Q}_i - Q_{e,i})/n_{pi}}{\sum_{j\in\mathcal{G}}(\overline{Q}_j - Q_{e,j})/n_{pj}}, \qquad i \in \mathcal{G}. \tag{3}$$

To adjust the speed of MG voltage response, a voltage-transient coefficient is added to the IPS model. In addition, the voltage regulation and reactive power sharing are compromised by a V-Q gain to achieve a common bus voltage and semi-equal reactive power sharing. This tuning process sets up a leader-follower relationship among DGs, where the equal voltages at DGs cause the improper difference of reactive power values. As depicted in Fig. 4(b), the V-Q compromise gain allows the voltage to deviate from the nominal value to share semi-equal reactive power values (Note that semi-equal signals x_i mean that $x_i \approx x_j, i \neq j$). Note that $\beta = 0$ eliminates the voltage regulation and $\beta = 1$ provides a highly voltage-regulating controller.

D. IPS Consensus for Virtual Impedance

The feeder impedance mismatch on the reactive power sharing causes the voltage drop across the line connected to DGs. Hence, this voltage drop deviates the output voltage from the nominal value. So as to ensure proper voltage regulation/stability, the virtual impedance is installed on DG terminal [19]. The virtual impedance damps the MG oscillations and decouples active and reactive power sharing with no power losses and efficiency degradation. As illustrated in Fig. 7, the proposed virtual impedance compensates the voltage drop across the feeder impedance with the active and reactive reference power P and Q of generator. The virtual resistance and reactance are implemented in dq-frame where Δv_d and Δv_q represent the

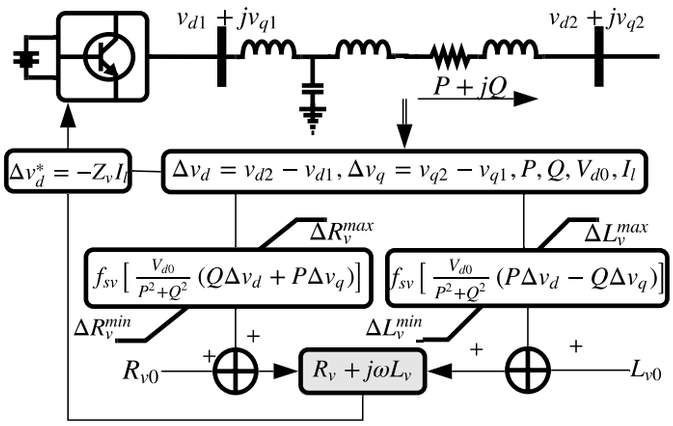

Fig. 7. Adaptive virtual impendance in IPS scheme.

voltage drop across the feeder impedance in both frames. The virtual impedance sensitivity function, f_{sv}, converts the inputs of deviation over calculated virtual resistance and inductance to smooth virtual impedance. This function is obtained from a sensitivity analysis of bus voltage with respect to the virtual impedance deviations [19]. The resistance and inductance changes are limited by the constraints of $[\Delta R_v^{min}, \Delta R_v^{max}]$ and $[\Delta L_v^{min}, \Delta L_v^{max}]$, respectively.

IV. Impact of IPS on Small-Perturbation Stability

Small-perturbation model is carried out using eigenvalue analysis with linearizing the islanded MG. Although this approach is only valid around the operating point, it presents the necessary condition of MG stability. To analyze the eigenvalue study, a small-signal state-space model of whole MG is obtained at a specific operation point. The whole MG state-space model is divided to three state-space sub-modules: generator, network, and load. In the following analysis, the individual inverter and SG models are established for the IPS control approach, and then combined to create the comprehensive generator state-space model. Finally, the combination of generator, network, and load state-space models obtains an MG state-space matrix.

A. State-Space Model of Individual Voltage Source Inverter

The voltage source inverter consists of power/voltage/current controllers, LCL filter, and coupling inductance [27]. Define voltage and current notations on d and q axis as follow:

$$x_{s,dq} = [x_{s,d} \quad x_{s,q}]^T, \quad x \in \{v, i\}, \quad s \in \{o, l\}. \tag{4}$$

To connect an inverter to the MG, the output variables $x_{s,qd}$ need to be converted to the common reference frame (DQ). The axis set (DQ) is the common reference frame rotating at frequency ω_{com}, whereas (dq_i) and (dq_j) are the reference frame of the ith and j^{th} inverters at ω_i and ω_j, respectively [28].
To provide a better understanding of the equation, the space-state model is given by

$$[\Delta\dot{x}] = A^{(g)}[\Delta x] + B^{(g)}[\Delta u_x] \tag{5}$$

$$[\Delta y] = C^{(g)}[\Delta x] + C_y^{(g)}[\Delta u_y], \tag{6}$$

$$g \in \{p, v, c, lcl, INV, SG, Ld, Ln\}$$

where $[\Delta y]$ is the output vector, and $[\Delta x]$ is the state vector of components in power/voltage/current controller in inverter, LCL filter, and inverter/SG/load/line sub-modules. Based on the model of the inverter presented in Section II, the state-space power controller model for an individual inverter can be written as

$$\begin{bmatrix} \Delta\dot{\theta} \\ \Delta\dot{P} \\ \Delta\dot{Q} \\ \Delta\dot{S}_v \end{bmatrix} = [A^{(p)}] \begin{bmatrix} \Delta\theta \\ \Delta P \\ \Delta Q \\ \Delta S_v \end{bmatrix} + [B^{(p)}] \begin{bmatrix} \Delta i_{l,dq} \\ \Delta v_{o,dq} \\ \Delta i_{o,dq} \end{bmatrix} + [B_{\omega_{com}}^{(p)}][\Delta\omega_{com}] \tag{7}$$

$$\begin{bmatrix} \Delta\omega \\ \Delta v_{o,dq}^* \end{bmatrix} = \begin{bmatrix} C_\delta^{(p)} \\ C_{PQ}^{(p)} \end{bmatrix} \begin{bmatrix} \Delta\theta \\ \Delta P \\ \Delta Q \\ \Delta S_v \end{bmatrix} \tag{8}$$

$$A^{(p)} = \begin{bmatrix} K & -m_p & 0 & 0 \\ 0 & -\omega_c & 0 & 0 \\ 0 & 0 & -\omega_c & 0 \\ 0 & 0 & 0 & 0 \end{bmatrix}, C_{PQ}^{(p)} = \begin{bmatrix} 0 & 0 & -n_q & -\kappa\beta \\ 0 & 0 & 0 & 0 \end{bmatrix} \tag{9}$$

$$B^{(p)} = \begin{bmatrix} 0 & 0 & 0 & 0 & 0 & 0 \\ 0 & 0 & \omega_c I_{o,d} & -\omega_c I_{o,q} & \omega_c V_{o,d} & \omega_c V_{o,q} \\ 0 & 0 & \omega_c I_{o,q} & -\omega_c I_{o,d} & \omega_c V_{o,q} & \omega_c V_{o,d} \\ 0 & 0 & 1 & 0 & 0 & 0 \end{bmatrix} \tag{10}$$

$$C_\delta^{(p)} = \begin{bmatrix} 0 & -m_p & 0 & 0 \end{bmatrix} \quad B_{\omega_{com}}^{(p)} = \begin{bmatrix} -1 & 0 & 0 & 0 \end{bmatrix}^T \tag{11}$$

where S_v is used to handle the integral over the voltage magnitude. Denote a difference between an individual inverter reference and the common reference frames by $\Delta\omega_{com}$.
Generally, the PID control is used for both voltage and current controllers to change line current magnitude flowing the coupling inductance. This line current change affects the reference voltage of inverter $v_{i,dq}$ by utilizing the slack variables γ_{dq} and υ_{dq} calculated by the integral over reference signals from power and voltage controllers. The virtual impedance $r_v + j\omega L_v$ is added to the current controller to regulate the output voltage. Under the virtual impedance paradigm, the algebraic equations for the current controller are given by

$$v_{i,d}^{new} = -r_v i_{l,d} + \omega L_v i_{l,q} + v_{i,d}^{old} \tag{12}$$

$$v_{i,q}^{new} = -r_v i_{l,q} - \omega L_v i_{l,d} + v_{i,q}^{old}. \tag{13}$$

The state-space models for the voltage/current controllers and LCL filter are given in [27]. A complete model of an individual inverter can be achieved by combining of state-space model of power controller, voltage/current controllers, and LCL filter. In total, there are 14 state variables, 3 inputs, and 2 outputs in each inverter model [28]:

$$[\Delta\dot{x}^{(INV)}] = [A^{(INV)}][\Delta x^{(INV)}] + [B^{(INV)}][\Delta v_{b,DQ}^{(INV)}] + [B_{\omega_{com}}^{(INV)}][\Delta\omega_{com}] \tag{14}$$

$$\begin{bmatrix} \Delta\omega^{(INV)} \\ \Delta i_{o,DQ}^{(INV)} \end{bmatrix} = \begin{bmatrix} C_\omega^{(INV)} \\ C_{i_{o,DQ}}^{(INV)} \end{bmatrix} [\Delta x^{(INV)}] \tag{15}$$

where the state variables are defined as follows:

$$\Delta x^{(INV)} = [\Delta\delta^{(INV)} \ \Delta P^{(INV)} \ \Delta Q^{(INV)} \ \Delta S_v^{(INV)} \ \Delta v_{dq}^{(INV)} \ \Delta\gamma_{dq}^{(INV)} \ \Delta i_{l,dq}^{(INV)} \ \Delta v_{o,dq}^{(INV)} \ \Delta i_{o,dq}^{(INV)}]^T. \tag{16}$$

B. State-Space Model of Individual SG

The SG model consists of stator and rotor windings, exciter, governor, turbine, and automatic voltage regulator which have been modelled in Section II. The small signal state space model of SG is given in [29], [30].

C. Complete Model of the Islanded MG

Models of all lines and loads are achieved from [27], [28]. A corresponding model of the islanded MG can be obtained by

combining the state-space models of generators, network, and loads through mapping matrices. These matrices connect output currents of generators or loads to nodes. Assume the bus in the islanded MG as a node, where generators and load exchange the current with it. To model the output voltage of each bus, a virtual resistor is assumed between each node and ground. This resistor is sufficiently large to have minimum influence on the dynamic MG stability [27]. Hence, the output voltage of the islanded MG with n_G generators connected together via n_{Ln} lines to meet the requirement of n_{Ld} loads, is given by

$$\begin{aligned}[\Delta v_{b,DQ}] =& R_N[M_{INV}[\Delta i_{o,DQ}] + M_{SG}[\Delta i_{o,DQ}] \\ &- M_{Ld}[\Delta i_{Ld,DQ}] + M_{Ln}[\Delta i_{Ln,DQ}]).\end{aligned} \tag{17}$$

The complete state-space model of the islanded MG is given by

$$\begin{bmatrix} \Delta\dot{x}^{(G)} \\ \Delta\dot{i}_{Ln,DQ} \\ \Delta\dot{i}_{Ld,DQ} \end{bmatrix} = [A^{(MG)}] \begin{bmatrix} \Delta x^{(G)} \\ \Delta i_{Ln,DQ} \\ \Delta i_{Ld,DQ} \end{bmatrix}, \tag{18}$$
$$[\Delta x^{(G)}] = [\Delta x^{(INV)} \otimes \Delta x^{(SG)}]$$

where $A^{(MG)}$ is given in (19). The MG stability is reflected by the eigenvalues of the matrix $A^{(MG)}$, which are determined by the characteristic equation $\Delta(\lambda)$:

$$\Delta(\lambda(k,\kappa)) = \lambda I_0 - A^{(MG)}, \quad \det\Delta(\lambda(k,\kappa)) = 0. \tag{20}$$

The eigenvalues are often referred to as modes, which reveal the different frequency components in the MG. Given $\Delta x^{(G)}$, the descriptor system is stable if all roots in (20) are in the open left-hand plane. Fig. 8 summarizes the IPS approach to share the active and reactive power as well as maintaining the frequency and voltage regulation. The IPS approach guarantees the MG stability with changing of the frequency and voltage controller gains. Care should be taken to tune these controller gains so as to ensure the overall MG stability margin more than the minimum threshold $\underline{S_m}$. Otherwise, the IPS approach sheds some loads when these gains are not effective. The S_m represents the stability margin loss/improvement due to any change in effective parameters or loading operating point. With Ψ_0 and Ψ_j defined as the stability margin in base load (no change in load) and loading condition with the change of jth controller gain, given by

$$\Psi = \underset{\lambda}{arg\,max}\,\mathbb{R}(\lambda(k,\kappa,n_p,m_p)), \quad S_m = \frac{\Psi_j}{\Psi_0} \times 100\,\%. \tag{21}$$

In general, the IPS parameters are very much dependent on the stability margin threshold. The relation between changes in IPS parameters and the MG stability determines the number of iteration.

V. Numerical Results

To validate the effectiveness of the proposed IPS controller, a modified CIGRE benchmark for a medium voltage network is implemented in MATLAB/SIMULINK. A general schematic of the CIGRE test case is shown in Fig. 9 [8]. This European medium-voltage benchmark features total installed DG capacity and the load of 3.8 and 1.5 MVA, respectively. The MG includes three diesel-based SGs connected to buses #1 and #3, one wind turbine (WT) in bus #11, and one battery in bus #6. The total rating power of SGs on bus #1 is 1200 kVA, and SG on bus #3 has the maximum nominal power 1000 kVA. The WT is a three blade HW43 with the rated power 600 kW and type of the SG model. The rated wind speed of the WT is 14.5 m/s [32]. The battery in bus #6 has a maximum power rating of 825 kW and a capacity of 6000 kWh. It is connected to AC link through a bidirectional voltage source inverter. The acceptable minimum state of charge (SOC) of the battery is 600 kWh. Feeders are connected together via 14 coupled π sections. For the purpose of this paper, the MG is assumed as a resistance dominated network. A detailed description of the test system and parameters is provided in [31]. This section is organized into four studies, starting with a characterization of the IPS control performance, and then examining the IPS control robustness under wind fluctuations, disconnection of DGs, and plug and play functionality.

A. Critical Eigenvalues Versus IPS Controller Parameters

Dominant eigenvalues are analyzed to evaluate the IPS impact on MG small-perturbation stability. These eigenvalues are determined from the procedure outlined in (19)-(20). The trajectory of dominant eigenvalues in the IPS approach is compared with that in the conventional droop controller (Base) under various controller gains. Assuming that initial MG parameters are obtained from the steady-state operating conditions in MATLAB/SIMULINK. The stability sensitivity index is defined to evaluate the MG stability in response to frequency and voltage controller gains $[K,\kappa,m_p,n_p]$. Generally, this is a manifestation of IPS robustness, which the dominant eigenvalue λ changes according to j^{th} controller gain x_j by $\partial\lambda/\partial x_j$. From Table I, it can be seen that the dominant eigenvalue is largely sensitive to the frequency and voltage control parameters in the base approach comparing to IPS gains. Increasing either feedback gains m_p or n_p to share active or reactive power results in an increasingly dominant eigenvalue change. Observe that the IPS controller is capable of providing the same power sharing with 50% improvement in the stability sensitivity index.

Fig. 10 compares the impact of the controller gains in the IPS approach, K,κ, with the base model, m_p,n_p, on the MG transient performance. To do this, the loads on all buses are changed in intervals around the steady-state equilibrium. In the base approach, the droop gains are changed to keep a uniform power sharing among DGs. Note that DGs with lower droop gains contribute more to the load changes. As depicted in Fig. 10, the dominant eigenvalues are strongly associated with the frequency control dynamics, while the overall damping of MG is dependent on eigenvalues of the voltage controller. From Fig. 10(a), it can be seen that as m_p decreases, the dominant eigenvalue reaches a point that for further increase in the gain the MG cannot remain in the stable region. Decreasing m_p of a single generator less than half of initial droop gain (m_{p0}), the dominant modes in the system are forced to the right side of root-locus coordination. As the same convention, with continuing the change of voltage droop gain (n_p), dominant eigenvalues move to the right side of root-locus coordination, leading to MG instability.

As observed in Fig.10, the corresponding IPS controller gains for frequency (K) and voltage (κ) are changed to achieve the same behavior of base approach. Increasing K and κ have effects nearly identical to decreasing m_p and n_p on power sharing, respectively. Traces of eigenvalues prove the robustness of IPS controller gains in response to load changes. Note that the IPS controller preserves the MG stability even though the droop gain change causes instability, while performing in the same operational mode.

In the base approach, S_m changes from 112% at $2m_{p0}$ to -85% (negative sign due to being in an unstable region) at $0.5m_{p0}$. To have the same power sharing behavior, the proposed IPS changes S_m from 104% at $0.8K_0$ to 80% at $1.6K_0$, thus demonstrating more robustness in frequency regulation than the base controller does.

To better evaluate the effectiveness of the IPS on voltage regulation, κ is changed from 0.75 to 2.5, while n_p changes from 32 to 0.5 times of nominal value n_{p0}. Note that a small droop gain is necessary to improve the transient response of DGs and share the power among them. This small droop gain reduces the stability margin with the

$$A^{(MG)} = \begin{bmatrix} A^{(G)} + B^{(G)} R_N M_G C^{(G)} & B^{(G)} R_N M_{Ln} & B^{(G)} R_N M_{Ld} \\ B^{(Ln)}_{v_{b,DQ}} R_N M_G C^{(G)} + B^{(Ln)}_{\omega} C^{(G)}_{\omega} & A^{(Ln)} + B^{(Ln)}_{v_{b,DQ}} R_N M_{Ln} & B^{(Ln)}_{v_{b,DQ}} R_N M_{Ld} \\ {}^{(Ld)}_{v_{b,DQ}} R_N M_G C^{(G)} + B^{(Ld)}_{\omega} C^{(G)}_{\omega} & B^{(Ld)}_{v_{b,DQ}} R_N M_{Ln} & A^{(Ld)} + B^{(Ld)}_{v_{b,DQ}} R_N M_{Ld} \end{bmatrix} \tag{19}$$

$$[X^{(G)}] = [X^{(INV)} \otimes X^{(SG)}], \quad X \in \{A, B, C, C_\omega\}, \quad R_N = \begin{cases} r_N, & i = j \\ 0, & i \neq j \end{cases}, \quad M_G(i,j) = \begin{cases} +1, & G_j \to node_i \\ 0, & otherwise \end{cases}$$

$$M_{Ld}(i,j) = \begin{cases} -1, & Ld_j \to node_i \\ 0, & otherwise \end{cases}, \quad M_{Ln}(i,j) = \begin{cases} -1, & i_{Ln_{(j,i)}} < 0, Ln_j \to node_i \\ +1, & i_{Ln_{(j,i)}} > 0, Ln_j \to node_i \\ 0, & otherwise \end{cases}$$

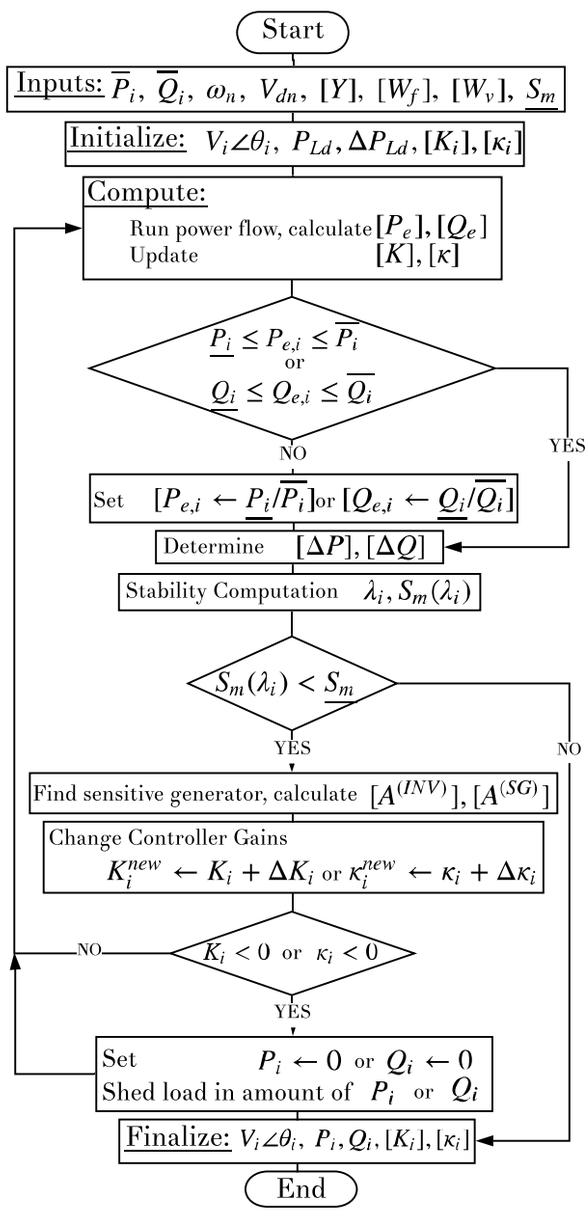

Fig. 8. Flowchart of the proposed IPS scheme.

growth of load and increases the reactive power sharing error to nominal values. Similar to the frequency control, the base model varies S_m from 125% in value of $32n_{p0}$ to 106% for $0.5n_{p0}$, whereas the IPS forces S_m from 124% at $0.75\kappa_0$ to 113% at $2.5\kappa_0$.

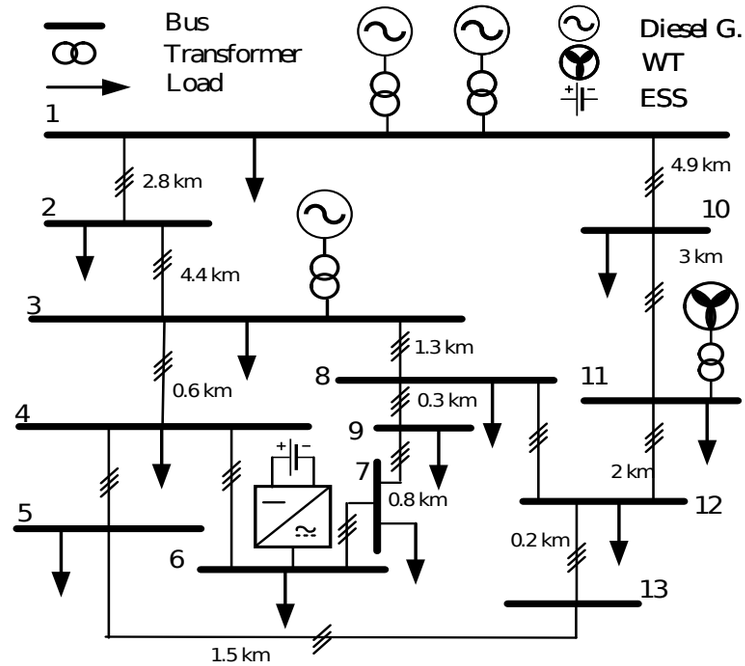

Fig. 9. 14-bus modified CIGRE benchmark of islanded MG [8].

TABLE I
DOMINANT EIGENVALUE SENSITIVITY.

	Frequency	Voltage
Base	$\partial\lambda/\partial m_p : 4.6$	$\partial\lambda/\partial n_p : 2.4$
IPS	$\partial\lambda/\partial k : 2.1$	$\partial\lambda/\partial\kappa : 1.6$

B. IPS Performance in Renewable Power Fluctuations (Scenario 1)

The effectiveness of IPS during renewable energy fluctuations is evaluated by comparing the MG response to wind power variations in both the base and IPS approaches. The wind power fluctuates between 15% and 35% of 800 kVA [31]. Fig. 11(a) shows the MG frequency dynamics for three cases: the IPS and the base model with/without ESS. First, considering the frequency dynamics in Fig. 11(a), controller gains quickly eliminate the frequency deviation experienced under the IPS approach. It causes the frequency regulation is maintained throughout wind fluctuation with minimal transients.
It is noted that ESS has a significant effect in compensating for the wind variations and that the active power output of diesel-based SGs undergoes no significant changes. Fig. 11(b) depicts the voltage profile of two buses in both base and IPS approaches. Observe that

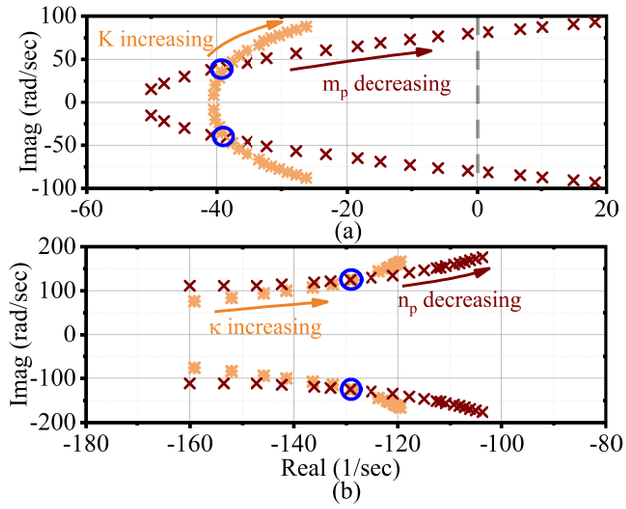

Fig. 10. Traces of eigenvalues as a function of base controller and corresponding IPS gains for (a) active power: $0.5m_{p0} \leq m_p \leq 2m_{p0}$, $0.8K_0 \leq K \leq 1.6K_0$; (b) reactive power: $0.5n_{p0} \leq n_p \leq 32n_{p0}$, $0.75\kappa_0 \leq \kappa \leq 2.5\kappa_0$. Blue circle indicates the steady-state operation.

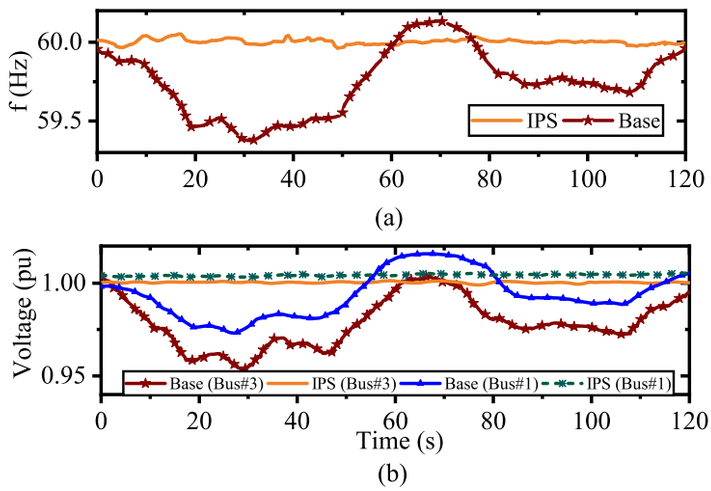

Fig. 11. (a) Frequency response and (b) voltage profiles for base and IPS models in variation of wind power (Scenario 1).

TABLE II
REACTIVE POWER SHARING AND VOLTAGE REGULATION ON BUS #3

	$\beta = 0$	$\beta = 0.5$	$\beta = 1$
Voltage (p.u.)	0.95	0.97	0.99
Reactive Power (kVAr)	430	417	395

the voltage variations in the IPS controller are preserved within the operating voltage range of 0.98-1.02 p.u. comparing to that in the base approach with ±0.05 p.u. voltage error. To elaborate the impact of Q-V compromise factor on the voltage regulation, a sensitivity analysis is performed on β in Table II. Increasing the feedback gain β results in an increasingly voltage regulation on bus #3, and decreases the reactive power sharing of diesel-based SG #3.

The ESS connected to bus #6 operates in the unity power factor under voltage source control paradigm; the discharging/charging ramp-rate is 30 MW/Hz, which is a zero power-frequency droop. To better evaluate the IPS controller, a frequency and voltage droop for the ESS is considered. Fig. 12(a) demonstrates that the diesel-based SGs make no contribution in the base approach, but have a significant commitment to generate the active power in the IPS controller. Observe in Fig. 12(b) that the ESS generates up to 800 kW of the active power and 40 kWh of total energy. When the wind

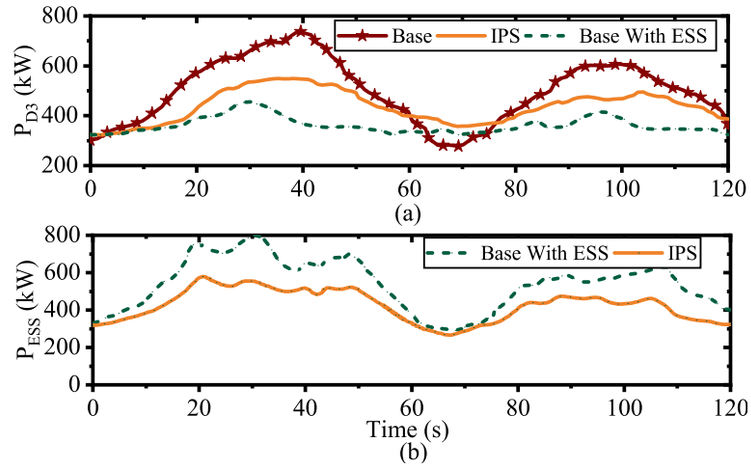

Fig. 12. Active power output of (a) diesel-based SG #3, (b) ESS due to wind power fluctuation (Scenario 1).

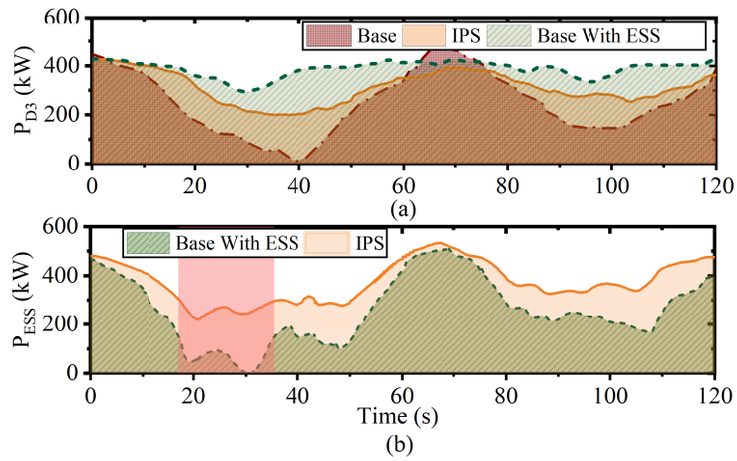

Fig. 13. Operating power capability of active power for (a) diesel-based SG, (b) ESS in wind power fluctuation (Scenario 1).

power continues fluctuating for an hour, sufficient ESS is needed to respond to the MG requirement. However, ESS implementation can be expensive, at normal prices, typically \$5-12k per kWh [8]. Active power sharing is precisely shared among diesel-based SGs and battery throughout the entire time-simulation. This power sharing behaviour is identical in all other studies, and hence the reactive power sharing plots are omitted due to space considerations.

Besides, small frequency droop gain forces ESS to dispatch significantly during the wind power fluctuations, while diesel-based SGs still have operating power capabilities to be dispatched. Fig. 13 shows the operating power capability of diesel-based SG #3 and ESS in three cases, respectively. Using the base with ESS approach, ESS reaches its rated power in t =[18 33]s, and there is no available power for the future dispatch. From Fig. 13(a), the diesel-based SG #3 has no contribution in active power sharing at t =40s, while the MG utilizes the ESS power significantly. Observe that IPS is capable of enhancing active power contribution of diesel-based SG #3 from 22% to 30%, and decreasing that in ESS from 48% to 37%. The rest of power contribution belongs to diesel-based SG #1. Without loss of generality, the IPS controller dispatches the active power among DGs to keep the operating power capability for all DGs uniformly. The voltage control performance of the base model is highly dependent on voltage droop gain (n_p). The impact of n_p on the voltage is shown in Fig. 14. As n_p decreases, the voltage variations are shifted up to reach the nominal value. Besides, it can be concluded that the adaptive virtual impedance quickly eliminates the voltage deviation of bus #3; thus, voltage regulation is maintained throughout wind

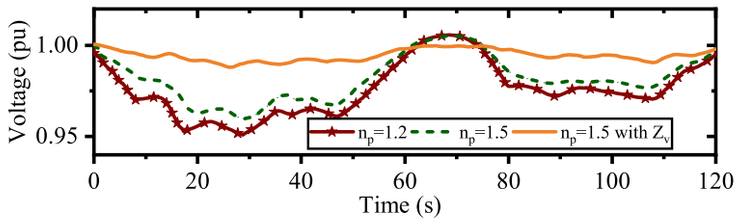

Fig. 14. The effectiveness of adaptive virtual impedance implementation on voltage output of buses (Scenario 1).

TABLE III
THE IMPACT OF IPS CONTROLLER GAINS ON POWER SHARING AND FREQUENCY VARIATION

IPS Gains	Load (kW)	Freq. (Hz)	Power (kW)[PF]%
K_{D1}, K_{D3}, K_{ESS}	ΔP_L	Δf	$\Delta P_{D1}, \Delta P_{D3}, \Delta P_{ESS}$
1,1,1	462	0.00004	68,150,244 [14,32,54]%
1.01,1,0.99	458	0.00007	74,149,235 [16,32,52]%
1.02,1,0.98	456	0.00002	88,147,221 [19,32,49]%
1.03,1,0.97	452	0.0012	93,146,213 [21,32,47]%
1.1,1,0.9	443	0.002	101,144,198 [23,33,44]%

power changes with minimal transients. The IPS controller equipped by the virtual impedance regulates the output voltages of buses via an integral-term. However, the reactive power sharing has an error Q_{err} $(= (Q_i - Q_{i0})/Q_{i0})$ around 4.2% and -3.1% for diesel-based SGs #1 and #3, respectively. Table III lists the power sharing among ESS and diesel-based SGs under inhomogeneous IPS controller gains. Control parameters except the IPS parameters are the same as Scenario 1. Note that these inhomogeneous controller gains result in varying transient frequency response, whereas the MG stability is unchanged. Due to the reactive characteristics of demand, the load power change from 462 kW to 443 kW. As illustrated in Table III, increasing the IPS controller gain for diesel-based SG #1 increases the active power of that DG from 68 kW to 101 kW, while ESS decreases its power contribution from 244 kW to 198 kW. However, once the ESS participation factor (PF) in active power sharing reaches 44% from 54%, the IPS controller is not capable of regulating the MG frequency close to zero steady-state error. The qualitative impacts of IPS controller gain on the MG transient performance and steady-state equilibrium are summarized in Table IV. The IPS controller offers several advantages as well as accurate power sharing and frequency and voltage regulation. Two transient coefficients of the IPS controller reduce the settling time of frequency and voltage regulation up to 20%. It can be seen that as these transient coefficients increase, the settling times reach some points that, for further increase in them, the settling times are unchanged. Note that the voltage response of the MG with Q-V compromise factor is significantly improved with a steady-state voltage around 0.99 p.u., whereas the reactive power sharing is not accurate.

C. IPS Performance in Disconnection of DGs (Scenario 2)

To better evaluate the performance of IPS during large disturbances, the diesel-based SG #1 is disconnected at t =1 s. Prior to this disconnection, the MG is assumed to be in a steady-state condition. For simplicity of analysis, the instantaneous active power output of the wind turbine is considered to be constant during the disconnection. Fig. 15 depicts the frequency response for the base model with/without ESS, and IPS. For the base model, the frequency drops below 59.7 Hz after the disconnection of DG, which is beyond the allowable frequency limit. The application of ESS improves the steady-state frequency around 59.9 Hz, while the frequency remains within acceptable limits; therefore, the MG does not need the load

TABLE IV
PERFORMANCE ANALYSIS IN CHANGING IPS CONTROLLER GAINS FOR SG #3

Gains	From	To	Analytical effect upon change
K_3	$0.8K_0$	$1.6K_0$	Increases P-sharing, S_m: 104%→ 80%
κ_3	$0.75\kappa_0$	$2.5\kappa_0$	Increase Q-sharing, S_m: 124%→ 113%
K_{tr}^f	0.5	1	Frequency regulation: t_{set}: 2.45 s→ 2 s
K_{tr}^v	0.5	1	Voltage regulation: t_{set}: 2.1 s→ 1.85 s
β_3	0.5	1	V_3: 0.97p.u.→ 0.99p.u., Q_{err}: 1.8%→2.4%

* The arrow (→) denotes gain change from an initial value to a final value.

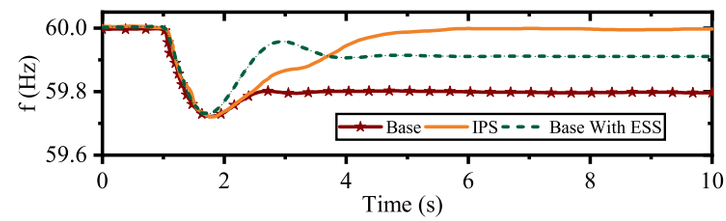

Fig. 15. Frequency response of MG during the disconnection of diesel-based SG #1 (Scenario 2).

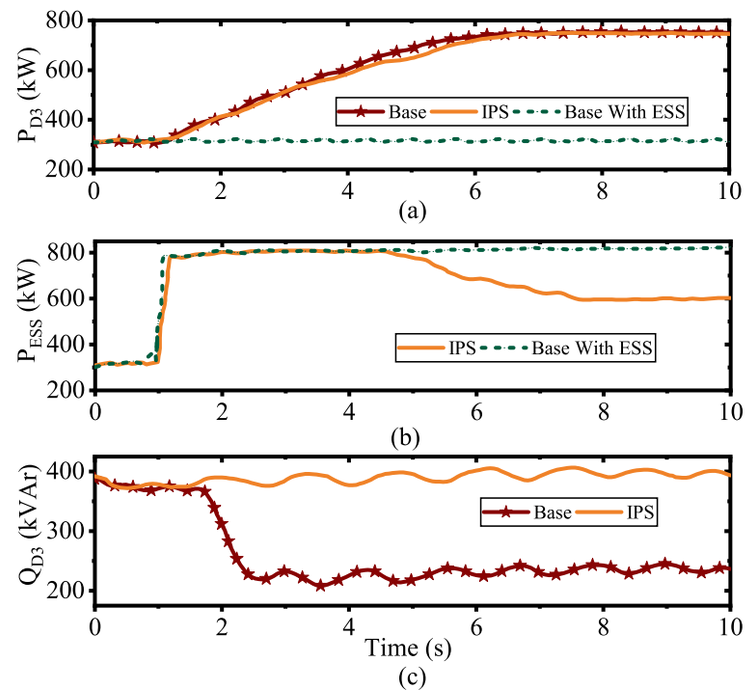

Fig. 16. Active power output of (a) diesel-based SG #3, (b) ESS, and (c) reactive power output of diesel-based SG #3 (Scenario 2).

curtailment. The IPS controller restores the frequency to the nominal value with a slightly higher settling time, as compared with the base model. Fig. 16 illustrates the corresponding active power output of diesel-based SG #3 after the disturbance at t =1 s. The fast-acting characteristics of ESS do not allow the diesel-based SG to operate during the disturbance in the base model; hence ESS does not exceed the maximum rating power 800 kW and 2 kWh energy in exchange of loads. Observe that for the base system with ESS, the diesel-based SG #3 has no significant change since the ESS compensates for the disconnection of SG #1. The IPS controller releases the operating power capability of ESS only 3 seconds after disturbance; thus, this controller forces diesel-based SG #3 to generate about 440 kW more than that in the base model with ESS. Fig. 16(c) presents the reactive power generated by diesel-based SG #3. Due to the voltage drop on buses, the reactive power generation of diesel-based SG #3

TABLE V
IPS PERFORMANCE UNDER PLUG AND PLAY OPERATION OF SG #1

	Base	Base With ESS	IPS
Frequency (Hz)	59.79	59.97	59.98
Voltage (p.u.)	0.94	0.95	0.99
ESS Utilization (kWh)	-	4.44	3.12

is decreased to 200 kVAr in the base approach. However, the IPS controller preserves the voltage magnitudes that remain within $\pm$ 0.05 p.u. voltage error.

D. Plug and Play Functionality of IPS Controller (Scenario 3)

The plug and play functionality is tested by disconnecting the diesel-based SG #1 at $t = 20$ s, and reconnecting at $t = 40$ s. A synchronization action is used in the downtime to synchronize the SG #1 with the remaining of the islanded MG before re-connection. Control parameters are the same as in Scenario 1. Two frequency and voltage indexes are defined to evaluate the IPS performance during this process. Table V shows that IPS controller reduces the frequency deviation, $\int_{20}^{40} |\Delta\omega(t)|dt$, during the plug and play functionality. In addition, it is concluded that the impact of this process on voltage deviation on bus #1, $\int_{20}^{40} |\Delta V_1(t)|dt$, is negligible for IPS approach comparing to base model. The ESS utilization are reported in Table V. Observe that using the IPS controller, the ESS utilization decreases by 30% and results in saving active energy around 1.32 kWh for each plug and play functionality. Without loss of generality, the IPS controller maintains accurate power sharing as well as frequency and voltage regulation despite the connection/disconnection of SG #1.

VI. Conclusion

In this paper, an intelligent power sharing (IPS) approach has been proposed for islanded MGs. Based on the realistic analysis and the simulation results shown in this paper, the IPS controller provides frequency and voltage regulation, while sharing power proportionally to the DGs' operating power capabilities and their droop control values. The IPS controller gains can be tuned to achieve either the voltage regulation, reactive power sharing, or a compromise between them. A mathematical model of small-perturbation stability has been presented along with performance analysis. By properly tuning the changes in IPS parameters, it has been demonstrated that the IPS provides zero steady-state errors in MG frequency and voltage, unlike conventional control models. This controller reduces the dependency on ESSs by distributing operating power capabilities of DGs over a wide time-horizon. Furthermore, the IPS controller decreases the impact of large disturbances on the MG, such as the disconnection of DGs and plug and play functionality. The IPS controller shows the robust frequency and voltage control performance under small perturbations with minimal transients.

Although the IPS controller brings technical advantages, it does not optimize MG operation from a viewpoint of cost or the ESS life-cycle. The design of optimal IPS control remains an open research problem. Besides, the IPS stability analysis has been achieved based on the MG parameter linearization, which is only valid around the operating conditions. Further investigation is needed to design a Lyapunov-based controller that guarantees the large-signal stability of frequency and voltage.

References

[1] T. Khalili, A. Jafari, M. Abapour, B. Mohammadi, "Optimal battery technology selection and incentive-based demand response program utilization for reliability improvement of an insular microgrid," *Energy*, vol.169, pp. 92-104, Feb. 2019.

[2] N. Rezaei, A. Ahmadi, A. H. Khazali and J. M. Guerrero, "Energy and frequency hierarchical management system using information gap decision theory for islanded microgrids," *IEEE Trans. Ind. Electron.*, vol. 65, no. 10, pp. 7921-7932, Oct. 2018.

[3] T. Khalili, M. Tarafdar, S. Gassemzadeh, S. Maleki, "Optimal reliable and resilient construction of dynamic self-adequate multi-microgrids under large-scale events," *IET Renewable Power Gen.*, vol. 13, pp. 1750-1760, July 2019.

[4] L. Olatomiwa, S. Mekhilef, M. Ismail, and M. Moghavvemi, "Energy management strategies in hybrid renewable energy systems: A review," *Renewable and Sustain. Energy Rev.*, vol. 62, pp. 821-835, Sep. 2016.

[5] T. Khalili, S. Nojavan, K. Zare, "Optimal performance of microgrid in the presence of demand response exchange: A stochastic multi-objective model," *Computers and Elec. Engineering*. vol. 74, pp.429-450, March 2019.

[6] A. Pappachen and A.P. Fathima "Critical research areas on load frequency control issues in a deregulated power system: A state of the art of review," *Renewable and Sustain. Energy Rev.*, vol. 72, pp. 163-177, May 2017.

[7] L. Huang, et al., "Transient stability analysis and control design of droop-controlled voltage source converters considering current limitation," *IEEE Trans. Smart Grid*, vol. 10, no. 1, pp. 578-591, Jan. 2019.

[8] M. Farrokhabadi, C. A. Canizares, and K. Bhattacharya, "Frequency control in isolated/islanded microgrids through voltage regulation," *IEEE Trans. Smart Grid*, vol. 8, no. 3, pp. 1185-1194, May 2017.

[9] Y. Khayat et al., "On the secondary control architectures of AC microgrids: An overview," *IEEE Trans. Power Electron.*, doi: 10.1109/TPEL.2019.2951694.

[10] A. Maulik and D. Das, "Optimal operation of droop-controlled islanded microgrids," *IEEE Trans. Sustain. Energy*, vol. 9, no. 3, pp. 1337-1348, July 2018.

[11] M. M. A. Abdelaziz, H. E. Farag, and E. F. El-Saadany, "Optimum reconfiguration of droop-controlled islanded microgrids," *IEEE Trans. Power Syst.*, vol. 31, no. 3, pp. 2144-2153, May 2016.

[12] F. Doost Mohammadi, H. Keshtkar, and A. Feliachi,"State-space modeling, analysis, and distributed secondary frequency control of isolated microgrids," *IEEE Trans. Energy Convers.*, vol. 33, no. 1, pp. 155-165, March 2018.

[13] S. Roozbehani, M.Tarafdar, and S. Ghassem, "Frequency control of islanded wind-powered microgrid based on coordinated robust dynamic droop power sharing," *IET Gen., Trans. Distr.*, vol. 13, no. 21, pp. 4968-4977, Nov. 2019.

[14] J. W. Simpson-Porco, Q. Shafiee, F. Dorfler, J. C. Vasquez, J. M. Guerrero, and F. Bullo, "Secondary frequency and voltage control of islanded microgrids via distributed averaging," *IEEE Trans. Ind. Electron.*, vol. 62, no. 11, pp. 7025-7038, Nov. 2015.

[15] M. Castilla, A. Camacho, J. Miret, M. Velasco, and P. Martin, "Local secondary control for inverter-based islanded microgrids with accurate active power sharing under high-load conditions," *IEEE Trans. Ind. Electron.*, vol. 66, no. 4, pp. 2529-2539, Apr. 2019.

[16] B. John, A. Ghosh and F. Zare, "Load sharing in medium voltage islanded microgrids with advanced angle droop control," *IEEE Trans. Smart Grid*, vol. 9, no. 6, pp. 6461-6469, Nov. 2018.

[17] Z. Li, Z. Cheng, Y. Xu, Y. Wang, J. Liang, and J. Gao, "Hierarchical control of parallel voltage source inverters in AC microgrids," *Journal of Engineering*, vol. 2019, no. 16, pp. 1149-1152, March 2019.

[18] T. V. Hoang and H. Lee, "An adaptive virtual impedance control scheme to eliminate the reactive power sharing errors in an islanding meshed microgrid," in *IEEE J. Emerging and Selected Topics in Power Electron.*, vol. 6, no. 2, pp. 966-976, June 2018.

[19] H. Mahmood, D. Michaelson, and J. Jiang, "Accurate reactive power Sharing in an islanded microgrid using adaptive virtual impedances," *IEEE Trans. Power Electron.*, vol. 30, no. 3, pp. 1605-1617, March 2015.

[20] H. Zhang, S. Kim, Q. Sun and J. Zhou, "Distributed adaptive virtual impedance control for accurate reactive power sharing based on consensus control in microgrids," *IEEE Trans. Smart Grid*, vol. 8, no. 4, pp. 1749-1761, July 2017.

[21] F. Zandi, B. Fani, I. Sadeghkhani, and A. Orakzadeh, "Adaptive complex virtual impedance control scheme for accurate reactive power sharing of inverter interfaced autonomous microgrids," *IET Gen., Trans. Dist.*, vol. 12, no. 22, pp. 6021-6032, Dec. 2018.

[22] J. M. Guerrero, J. C. Vasquez, J. Matas, L. G. de Vicuna, and M. Castilla, "Hierarchical control of droop-controlled AC and DC microgrids: A general approach toward standardization," *IEEE Trans. Ind. Electron.*, vol. 58, no. 1, pp. 158-172, Jan. 2011.

[23] R. Majumder, "Some aspects of stability in microgrids," *IEEE Trans. Power Syst.*, vol. 28, no. 3, pp. 3243-3252, Aug. 2013.

[24] F. Mumtaz, M. H. Syed, M. A. Hosani, and H. H. Zeineldin, "A novel approach to solve power flow for islanded microgrids using modified newton raphson with droop control of DG," *IEEE Trans. on Sustain. Energy*, vol. 7, no. 2, pp. 493-503, April 2016.

[25] P. Kundur, J.B.Neal, and G.L. Mark. *Power system stability and control*. McGraw-hill, 1994.

[26] A. J. Collin, G. Tsagarakis, A. E. Kiprakis, and S. McLaughlin, "Development of low-voltage load models for the residential load sector," *IEEE Trans. Power Syst.*, vol. 29, no. 5, pp. 2180-2188, Sep. 2014.

[27] N. Pogaku, M. Prodanovic, and T. C. Green, "Modeling, analysis and testing of autonomous operation of an inverter-based microgrid," *IEEE Trans. Power Electron.*, vol. 22, no. 2, pp. 613-625, March 2007.

[28] H. Liang, B. J. Choi, W. Zhuang and X. Shen, 'Stability enhancement of decentralized inverter control through wireless communications in microgrids," *IEEE Trans. Smart Grid*, vol. 4, no. 1, pp. 321-331, March 2013.
[29] X. Tang, W. Deng, and Z. Qi, "Investigation of the dynamic stability of microgrid," *IEEE Trans. Power Syst.*, vol. 29, no. 2, pp. 698-706, March 2014.
[30] P. C. Krause. *Analysis of electric machinery*. McGraw-Hill, 1986.
[31] M. Farrokhabadi, C. A. Canizares, and K. Bhattacharya, "Unit commitment for isolated microgrids considering frequency control," *IEEE Trans. Smart Grid*, vol. 9, no. 4, pp. 3270-3280, July 2018.
[32] "HW43 600 kW (Hewind)", *Wind Power*, Jan.2020. [Online]. Available: https://www.thewindpower.net/scripts/fpdf181/turbine.php?id=719

Mehdi Parvizimosaed (S'17) received the B.Sc. degree in electrical engineering from Iran University Science and Technology, Tehran, Iran, in 2012, and the M.Sc. degree in electric power engineering from University of Tehran, Tehran, Iran, in 2015. He is currently pursuing the Ph.D. degree in the Department of Electrical and Computer Engineering, University of Waterloo, Waterloo, ON, Canada, since 2016.
His current research interests include modelling, control, and operation of smart microgrids.

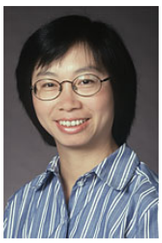

Weihua Zhuang (M'93-SM'01-F'08) has been with the Department of Electrical and Computer Engineering, University of Waterloo, Waterloo, ON, Canada, since 1993, where she is a Professor and a Tier I Canada Research Chair in Wireless Communication Networks.
Dr. Zhuang was a recipient of the 2017 Technical Recognition Award from the IEEE Communications Society Ad Hoc and Sensor Networks Technical Committee, and a co-recipient of several Best Paper Awards from IEEE conferences. She was the Editor-in-Chief of the IEEE TRANSACTIONS ON VEHICULAR TECHNOLOGY from 2007 to 2013, the Technical Program Chair/Co-Chair of IEEE VTC Fall 2017 and Fall 2016, and the Technical Program Symposia Chair of IEEE Globecom 2011. She is an elected member of the Board of Governors and Vice President - Publications of the IEEE Vehicular Technology Society. She was an IEEE Communications Society Distinguished Lecturer from 2008 to 2011. Dr. Zhuang is a Fellow of the Royal Society of Canada, the Canadian Academy of Engineering, and the Engineering Institute of Canada.